ACS Sustainable Chemistry & Engineering

pubs.acs.org/journal/ascecg

Research Article

High-Density Iron−Nickel Dual Sites in Carbon Aerogels as Effective Alkaline Water/Seawater Oxidation Electrocatalysts

Linshu Shan,[#] Yang Liu,[*,#] Yang Chen, Xinjie Zhang, Haizhong Dai, Dahai Xu, Bingzhe Yu, Yi Zhang, Shaowei Chen,[*] Ting He,[*] and Xiaoping Ouyang

Cite This: *ACS Sustainable Chem. Eng.* 2025, 13, 311−320

Read Online

ACCESS | Metrics & More | Article Recommendations | Supporting Information

ABSTRACT: Carbon-based nanocomposites with atomically dispersed transition metals have been found to exhibit excellent electrocatalytic activity toward the oxygen evolution reaction (OER). Yet, the low metal loads and severe electrooxidation of carbon greatly limit the activity and stability. Reducing the pyrolysis temperature can weaken the aggregation of metal atoms, and using carbon aerogel as a 3D scaffold can maximize accessible metal sites. Simultaneously, a lower pyrolysis temperature can provide a higher oxygen content for the carbon substrate and enhance resistance against electrooxidation. Herein, carbon aerogels embedded with Fe−Ni dual atom centers (NCA/FeNi-500) are synthesized by controlled pyrolysis at 500 °C of a chitosan hydrogel composite along with $FeCl_3$ and $NiCl_2$. With an atomically dispersed metal loading of 4.35 wt %, NCA/FeNi-500 exhibits a remarkable OER catalytic activity in both alkaline water and simulated alkaline seawater, featuring a low overpotential of only +294 and +306 mV to reach the current density of 10 mA cm^{-2}, respectively, along with excellent long-term stability during overall water splitting, a performance much better than those with commercial RuO_2. First-principles calculations show that adjacent NiN_4 sites effectively promote the OER kinetics at FeN_4 sites by reducing the energy barrier of O−O formation. This is also manifested in alkaline saline water splitting.

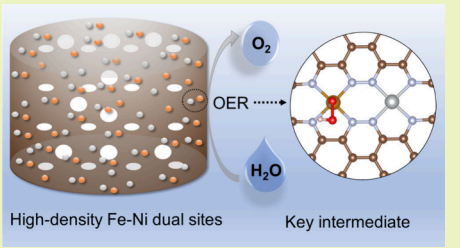

KEYWORDS: *dual-atom catalyst, carbon aerogels, oxygen evolution reaction, water splitting, seawater oxidation*

INTRODUCTION

Noble metal oxides (e.g., RuO_2 and IrO_2) have been the catalysts of choice for the oxygen evolution reaction (OER),[1,2] a critical process in hydrogen production from water splitting. However, their high cost and poor stability hamper their large-scale application. Therefore, development of low-cost, high-performance OER electrocatalysts has become a research hotspot in recent years.[3−5] Carbon-based nanocomposites with atomically dispersed transition metal centers have been found to exhibit good OER activity, but the actual catalytic performance is far below the theoretical expectation, due in part to the limited metal loading and stability. These nanocomposite catalysts are usually obtained by pyrolysis at high temperatures to stabilize metal single atom sites and improve electroconductivity; yet, metal atoms are prone to aggregation at high temperatures, such that the loading of the atomic sites is typically below 2 wt %.[6−8] The loading issue can be mitigated by various strategies: (i) anchoring metal atoms by ligands with N, S, or O atoms, (ii) spatial confinement by microporous defects in soft/hard templates, and (iii) optimization of thermal treatment by regulating heating temperature, annealing rate, and atmosphere, among others.[9−11] Nevertheless, even with a high metal loading, such carbon-based nanocomposites may still show an unsatisfactory catalytic performance, because part of the metal sites are embedded within the carbon interior with minimal accessibility.[12] Therefore, it remains a key challenge to increase the metal loading of carbon-based nanocomposites and simultaneously maximize the accessibility of the metal sites.

This can be resolved by appropriately reducing the pyrolysis temperature so as to impede the aggregation of metal atoms and increase the metal loading and by using porous carbon aerogel as the substrate to maximize the atomic dispersion of the metal sites. Additionally, a reduced pyrolysis temperature leads to a high oxygen content of the carbon scaffold, which can improve the resistance against carbon oxidation during electrolysis. In this study, we choose biomass hydrogels containing metal-chelating ligands as the templates to prepare carbon aerogels with iron−nickel dual atomic sites (NCA/FeNi-500) at a low pyrolysis temperature of 500 °C.[13,14] Results from microscopic and spectroscopic measurements show that FeN_4 and NiN_4 moieties are uniformly dispersed into the carbon aerogels with indirect chemical bonds.[15] First-principles calculations show that the adjacent NiN_4 sites can

Received: September 2, 2024
Revised: December 18, 2024
Accepted: December 18, 2024
Published: January 3, 2025

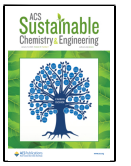

https://doi.org/10.1021/acssuschemeng.4c07297
ACS Sustainable Chem. Eng. 2025, 13, 311−320

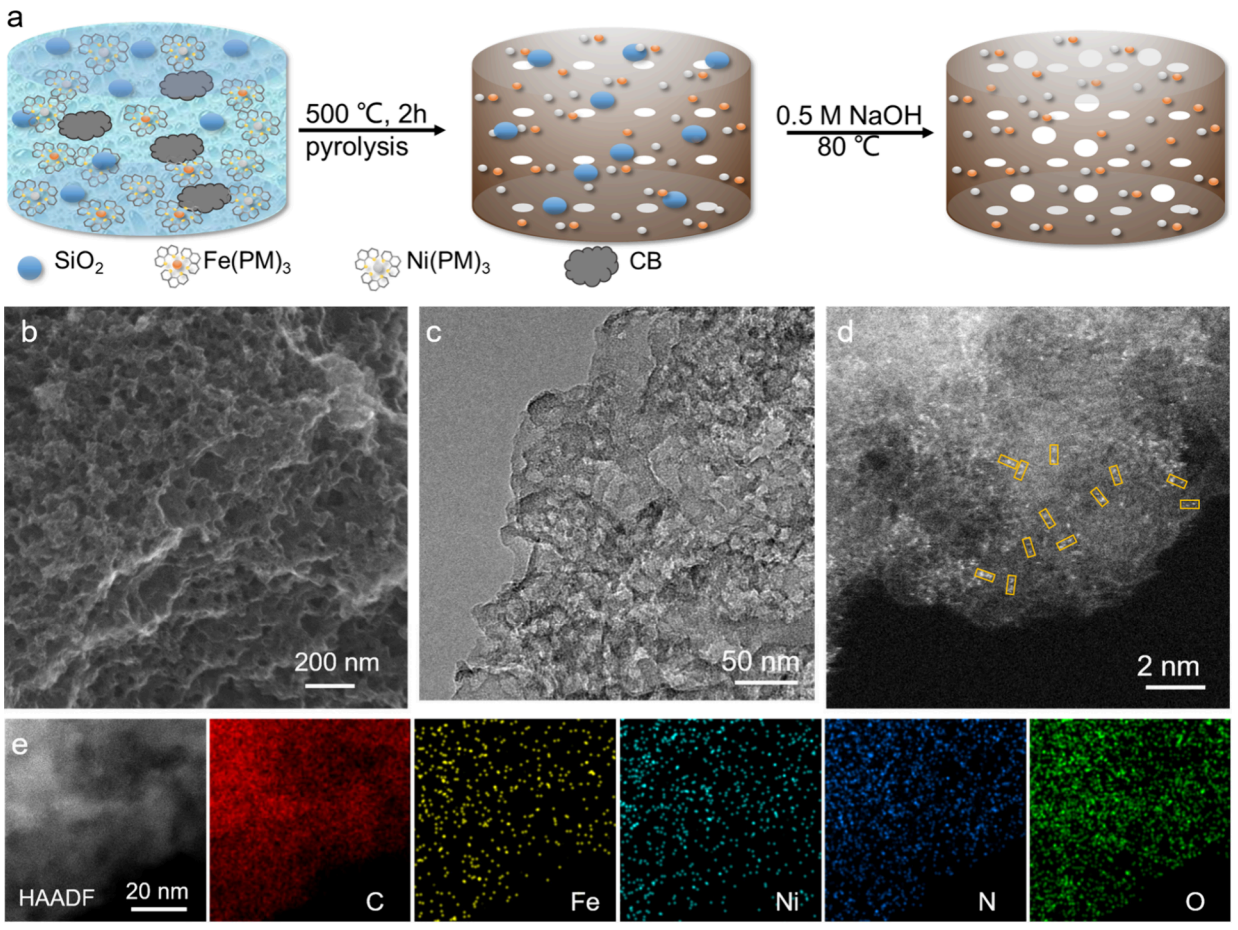

Figure 1. (a) Schematic illustration of the preparation of NCA/FeNi-500 carbon aerogels. (b) SEM and (c) TEM images of NCA/FeNi-500. (d) HAADF-STEM image and (e) corresponding elemental mapping image of NCA-FeNi-500.

effectively promote the OER activity of the FeN_4 moieties by reducing the energy barrier of O−O formation. Electrochemically, NCA/FeNi-500 indeed exhibits not only an excellent OER activity, with a respective overpotential of +294 and +306 mV at 10 mA cm^{-2} in alkaline water and simulated alkaline seawater, but also remarkably enhanced stability during overall water splitting, as compared to the commercial RuO_2 benchmark.

EXPERIMENTAL SECTION

Materials. Silicon dioxide (SiO_2) nanoparticles (15 nm), iron(II) chloride tetrahydrate ($FeCl_2{\cdot}4H_2O$), nickel(II) acetate tetrahydrate ($Ni(CH_3COO)_2{\cdot}4H_2O$), cobalt(II) acetate tetrahydrate ($Co(CH_3COO)_2{\cdot}4H_2O$), acetic acid ($CH_3COOH$), potassium hydroxide (KOH), sodium chloride (NaCl), ethylenediaminetetraacetic acid (EDTA), 1,10-phenanthroline monohydrate (PM), and sodium hydroxide (NaOH) were purchased from Aladdin Reagents (Shanghai, China). Chitosan, ruthenium(IV) oxide (RuO_2), and 5% Nafion solution were purchased from Sigma-Aldrich (USA). Polytetrafluoroethylene (PTFE, 60 wt %) was purchased from Daikin (Japan). Pt/C (20 wt %) was purchased from Tanaka (Japan). Acetylene black was purchased from Sinero (Suzhou, China). All other reagents were of analytical grade, and ultrapure water was used throughout the study.

Preparation of Hydrogel Precursor. Chitosan (60.0 mg) and SiO_2 (40.0 mg) were dispersed in 3 mL of a 1 wt % acetic acid solution under magnetic stirring to produce liquid A. Then, 5.9 mg of PM was dispersed in 80 μL of a $FeCl_2$ (0.2 M) solution to prepare the $Fe(PM)_3$ metal complex, and 14.8 mg of PM was dispersed in 200 μL of a $Ni(CH_3COO)_2$ (0.2 M) solution to prepare the $Ni(PM)_3$ metal complex. These metal complexes and 6.0 mg of conductive carbon black were then added to liquid A under magnetic stirring before being frozen at −20 °C for 12 h to obtain a hydrogel precursor.

Sample Preparation. The hydrogel precursor prepared above was freeze-dried for 15 h to obtain a dry gel before pyrolysis at 500 °C for 2 h in an Ar atmosphere at a heating rate of 5 °C min^{-1}, followed by cooling at the same rate. After pyrolysis, the sample was slightly ground, dispersed in 20 mL of 0.5 M NaOH in an 80 °C water bath under magnetic stirring for 2 h to remove SiO_2, and then washed with ultrapure water and ethanol and dried in an oven at 60 °C for 80 min, yielding the final aerogel product that was denoted as NCA/FeNi-500.

A series of comparative samples were prepared in the same manner except for the following differences: (1) NCA/Fe-500 without the addition of $Ni(PM)_3$, NCA/Ni-500 without the addition of $Fe(PM)_3$, and NCA-500 without either metal complex, (2) NCA/FeCo-500 with the addition of $Fe(PM)_3$ and $Co(PM)_3$ and NCA/NiCo-500 with the addition of $Ni(PM)_3$ and $Co(PM)_3$, (3) CA/FeNi-500 by using $Fe(EDTA)_3$ and $Ni(EDTA)_3$ as metal complexes instead of $Fe(PM)_3$ and $Ni(PM)_3$. In these syntheses, the relevant metal complexes were prepared by dispersing the metal salts into the PM or EDTA solution.

Details of structural characterization of the samples are included in the Supporting Information.

Electrochemistry. OER tests were carried out using a three-electrode system in 1.0 M KOH. The reference electrode was a Ag/AgCl electrode, and the counter electrode was a platinum sheet. The working electrode was composed of two layers: a nickel foam layer and a catalyst layer. The nickel foam was washed by ultrasound treatment in 0.2 M HCl, ultrapure water, and ethyl alcohol, successively. To prepare the catalyst layer, 6 mg of the nano-

https://doi.org/10.1021/acssuschemeng.4c07297
ACS Sustainable Chem. Eng. 2025, 13, 311−320

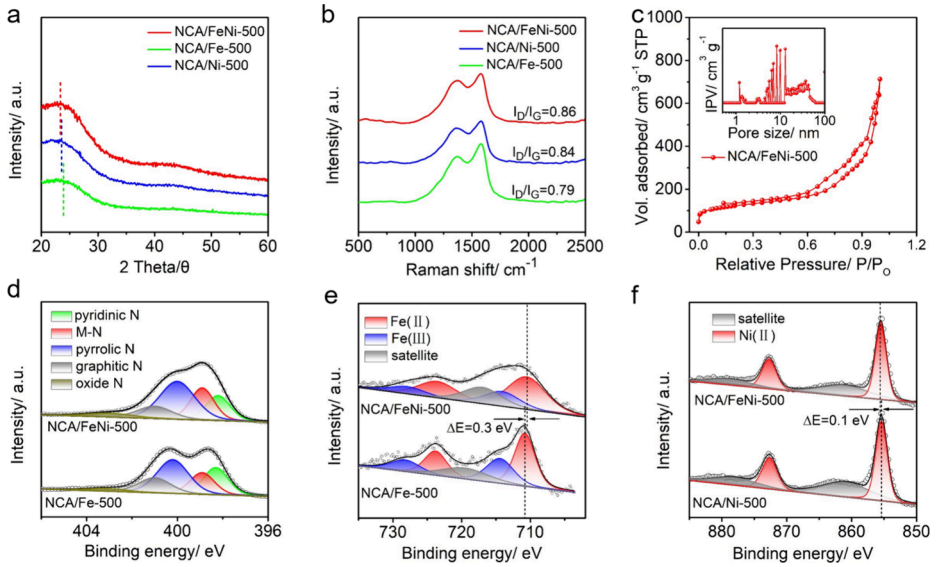

Figure 2. (a) XRD patterns and (b) Raman spectra of NCA/FeNi-500, NCA/Fe-500, and NCA/Ni-500. (c) Nitrogen adsorption and desorption isotherms of NCA/FeNi-500. Inset of panel (c) is the pore size distribution. High-resolution scans of the (d) N 1s, (e) Fe 2p, and (f) Ni 2p electrons of the samples.

composites prepared above, 3 mg of acetylene black, and 5 μL of PTFE were first mixed in ethyl alcohol, ground uniformly, and rolled into a 1.0 cm × 2.0 cm sheet. The sheet was cut into 0.5 cm × 0.5 cm pieces and transferred onto the nickel foam. The total thickness of the working electrode was ca. 0.3 mm after compression with a manual tablet machine, which was dried with an infrared lamp for 30 min.

The overall water electrolysis test was carried out using commercial Pt/C as the cathode catalyst and NCA/FeNi-500 or commercial RuO_2 as the anode catalysts. The cathode and anode working electrodes were prepared in the same way as the working electrode in the OER test. The mass loading was 3 mg cm^{-2} for NCA/FeNi-500, 1 mg cm^{-2} for Pt/C, and 1 mg cm^{-2} for RuO_2.

RESULTS AND DISCUSSION

Sample Synthesis and Structural Characterization. The sample synthesis is schematically illustrated in Figure 1a. Briefly, hydrogel precursors were prepared by mixing a chitosan/SiO_2 sol with Fe(PM)$_3$ and Ni(PM)$_3$ complexes (Figure S1), followed by lyophilization, low-temperature pyrolysis, and NaOH etching to produce the NCA/FeNi-500 carbon aerogels. In scanning electron microscopy (SEM) and transmission electron microscopy (TEM) measurements (Figure 1b, c), one can see that the sample possessed a large number of cavities within the carbon scaffold but no metal nanoparticles. A similar morphology was observed for NCA/Fe-500 and NCA/Ni-500 (Figure S2). Consistent results were obtained from high-angle annular dark-field scanning TEM (HAADF-STEM) measurements, where a number of bright spots can be readily solved against the low-contrast scaffold, suggesting atomic dispersion of the Fe and Ni species within the carbon matrix (Figure 1d). In elemental mapping based on energy-dispersive X-ray spectroscopy (EDS), the elements of C, N, O, Fe, and Ni can indeed be seen to be uniformly dispersed within the carbon scaffold (Figure 1e).

Further structural insights were obtained from X-ray diffraction (XRD) measurements. From Figure 2a, NCA/FeNi-500, NCA/Fe-500, and NCA/Ni-500 can all be seen to consist of two broad diffraction peaks at $2\theta \approx 26°$ and 44° due to the (002) and (100) planes of graphitized carbon (PDF#41-1487). The absence of additional diffraction features suggests that the samples were free of crystalline metal (oxide) nanoparticles. The corresponding Raman spectra are shown in Figure 2b, where the samples all exhibit a D band at 1360 cm^{-1} and a G band at 1580 cm^{-1}. The ratio of the D and G band intensity (I_D/I_G) was very close at 0.86 for NCA/FeNi-500, 0.79 for NCA/Fe-500, and 0.84 for NCA/Ni-500, suggestive of a slightly more defective structure of NC/FeNi-500 as compared to the others.[16] In nitrogen sorption measurements (Figure 2c), NCA/FeNi-500 shows a Type IV isotherm with an obvious adsorption hysteresis loop, implying a mesopore-rich structure. In fact, from the pore size distribution in the inset to Figure 2c, the sample can be seen to consist of micropores, mesopores, and macropores, with major peaks at 1.3, 10, and 50 nm, suggesting the formation of a hierarchical porous structure. Note that this is conducive to mass transfer of OER.[17]

X-ray photoelectron spectroscopy (XPS) measurements were then carried out to examine the elemental composition and valence states of the samples. From the survey spectra in Figure S3, one can see that the NCA/FeNi-500, NCA/Fe-500, and NCA/Ni-500 samples contained ca. 82 at% C, 8 at% O, and 9 at% N, along with a slightly different metal content (1.08 at% for NCA/FeNi-500, 1.03 at% for NCA/Ni-500, and 0.36 at% for NCA/Fe-500) (Table S1). It should be noted that such a high content of heteroatoms, such as O and N, would enhance the hydrophilicity of the carbon scaffold, which facilitates the adsorption of water molecules (as reactants) and accelerates diffusion of oxygen molecules (as products) during OER (vide infra).[18,19] Notably, the oxygen content increased from 4.36 to 8.26 at% as the pyrolysis temperature decreased from 900 to 500 °C (Table S2 and Figure S4), and a higher oxygen content in the carbon substrate is known to enhance resistance against electrooxidation of carbon. Meanwhile, the metal contents were consistent with results from the inductively coupled plasma-optical emission spectrometry (ICP-OES) measurements, where the total metal content (4.35 wt %) of NCA/FeNi-500 was somewhat higher than those of NCA/Fe-500 (1.46 wt %) and NCA/Ni-500 (3.20 wt %) (Table S3).

https://doi.org/10.1021/acssuschemeng.4c07297
ACS Sustainable Chem. Eng. 2025, 13, 311−320

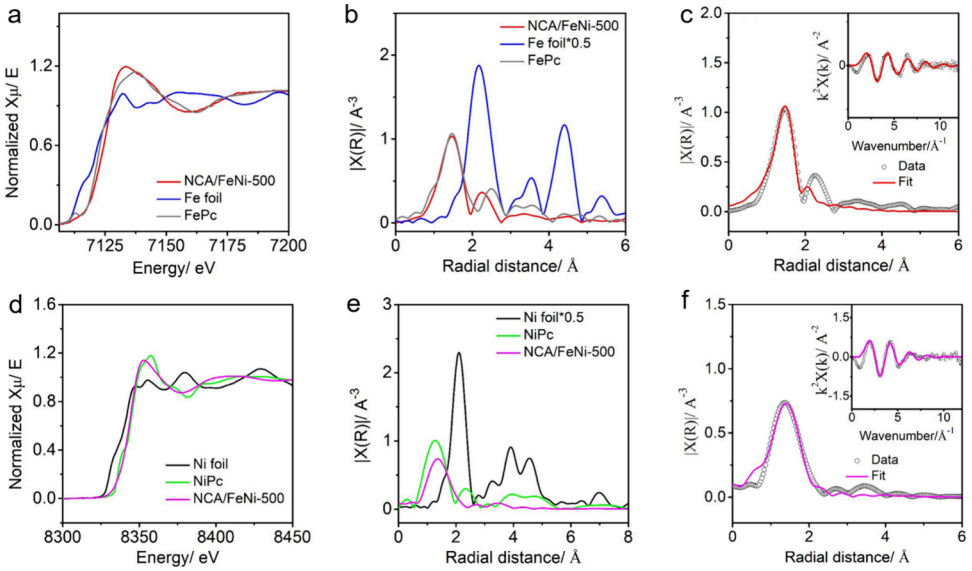

Figure 3. (a) Fe K-edge XANES spectra of NCA/FeNi-500, FePc, and Fe foil and (b) the corresponding R-space EXAFS profiles. (c) Fitting of the Fe EXAFS profile of NCA/FeNi-500 (inset is the K-space profiles), (d) Ni K-edge XANES spectra of NCA/FeNi-500, NiO, and Ni foil, and (e) the corresponding R-space EXAFS profiles. (f) Fitting of the Ni EXAFS profile of NCA/FeNi-500 (inset is the K-space profiles).

The high-resolution scans of the C 1s electrons are shown in Figure S5. NCA/FeNi-500 can be seen to possess an sp^3 content of 25.1 at%, slightly higher than those for NCA/Ni-500 (23.3 at%) and NCA/Fe-500 (21.3 at%) (Table S4), in good agreement with results from Raman measurements (Figure 2b). The high-resolution O 1s spectra of the oxidation phase are shown in Figure S6, where the absence of the metal−oxygen (M−O) peak below 530 eV suggests that no metal oxide was formed in the samples (Table S5). In Figure 2d and Figure S7, the high-resolution N 1s spectra can be deconvoluted into five N species, pyridinic N at 398.2 eV, metal-N at 399.0 eV, pyrrolic N at 400.0 eV, graphitic N at 401.0 eV, and oxidized N at 403.1 eV,[20] suggesting the formation of metal, N-codoped carbon aerogels in the form of MN_x coordination moieties. From Table S6, NCA/FeNi-500 can be seen to possess a much higher content of metal-N (2.09 at%) than NCA/Ni-500 (1.85 at%) and NCA/Fe-500 (1.67 at %). The Fe 2p spectra are shown in Figure 2e, where the doublets at ca. 711/724 eV and 714/728 eV can be ascribed to the $2p_{3/2}/2p_{1/2}$ electrons of Fe(II) and Fe(III), respectively,[21] and the fraction of Fe(II) is 63.2% in NCA/FeNi-500, slightly higher than that of NCA/Fe-500 (61.6%). From the Ni 2p spectra in Figure 2f, both NCA/FeNi-500 and NCA/Ni-500 can be seen to contain only Ni(II), with a doublet at ca. 856/873 eV.[22] Notably, the Fe 2p binding energy of NCA/FeNi-500 can be seen to show a negative shift of ca. 0.3 eV while the Ni 2p binding energy shows a positive shift of ca. 0.1 eV (Table S7), as compared to the monometallic counterparts of NCA/Fe-500 and NCA/Ni-500, respectively, suggesting electron transfer from Ni to Fe in NCA/FeNi-500.

The atomic configurations of the Fe and Ni sites in NCA/FeNi-500 were further investigated by X-ray absorption spectroscopy (XAS) measurements. From the X-ray near edge absorption spectroscopy (XANES) profiles in Figure 3a, the Fe K-edge energy of NCA/FeNi-500 can be seen to be close to that of iron(II) porphyrin (FePc), but deviate markedly from that of Fe foil; in addition, in the corresponding extended X-ray absorption fine structure spectroscopy (EXAFS) profiles, the postedge oscillation patterns showed an apparent overlap between NCA/FeNi-500 and FePc, but differed drastically from that of Fe foil. These indicate that the Fe valence state of NCA/FeNi-500 was close to +2, and the Fe centers were predominantly in the planar tetragonal configuration that is analogous to that of FePc.

In fact, from the Fourier-transform EXAFS (FT-EXAFS) profiles in Figure 3b, the Fe−N path can be clearly identified at 1.4 Å for NCA/FeNi-500 and FePc, and the peak at ca. 2.3 Å can be ascribed to the second shell of single Fe atoms,[10,23−27] whereas the Fe−Fe peak at 2.2 Å in Fe foil is absent in NCA/FeNi-500. This confirms atomic dispersion of Fe within NCA in the form of FeN_x and no Fe nanoparticles in NCA/FeNi-500. The Ni centers in NCA/FeNi-500 were also investigated in the same manner. As illustrated in Figure 3d, the Ni K-edge energy in NCA/FeNi-500 is different from that of Ni foil but similar to that of NiPc, suggesting a valence state close to +2. FT-EXAFS measurements (Figure 3e) show a Ni−N peak at 1.4 Å,[28] but no Ni−Ni peaks at 2.2 Å. These results indicate that Ni in NCA/FeNi-500 is also atomically dispersed in the form of NiN_x.

The coordination number (CN) and bond length of the Fe and Ni centers were then quantitatively examined by fitting of the EXAFS data (Figure 3c, f), and the results are listed in Table S8. One can see that the bond length of Fe−N is ca. 1.98 Å with a CN of 3.8, whereas it is 2.02 Å for Ni−N with a CN of 3.7. These indicate that both Fe and Ni centers were mostly coordinated by 4 N atoms forming a MN_4 configuration in the carbon aerogels. Note that in the above XPS measurements, the Fe−Ni electron transfer interactions suggest a fairly close proximity between Fe and Ni. This implies that these two atoms likely coexist in the form of indirect chemical bonds, namely, FeN_4−NiN_4 (Figure 4a),[15] consistent with the adjacent atomic pairs observed in HAADF-STEM measurements (Figure 1d).

Theoretical Study. First-principles calculations (details in the Supporting Information) were then performed to investigate and compare the OER activity of the dual/single metal sites within a carbon matrix, namely, FeN_4−NiN_4, FeN_4, and NiN_4. The optimized configurations of these atomic sites

https://doi.org/10.1021/acssuschemeng.4c07297
ACS Sustainable Chem. Eng. 2025, 13, 311−320

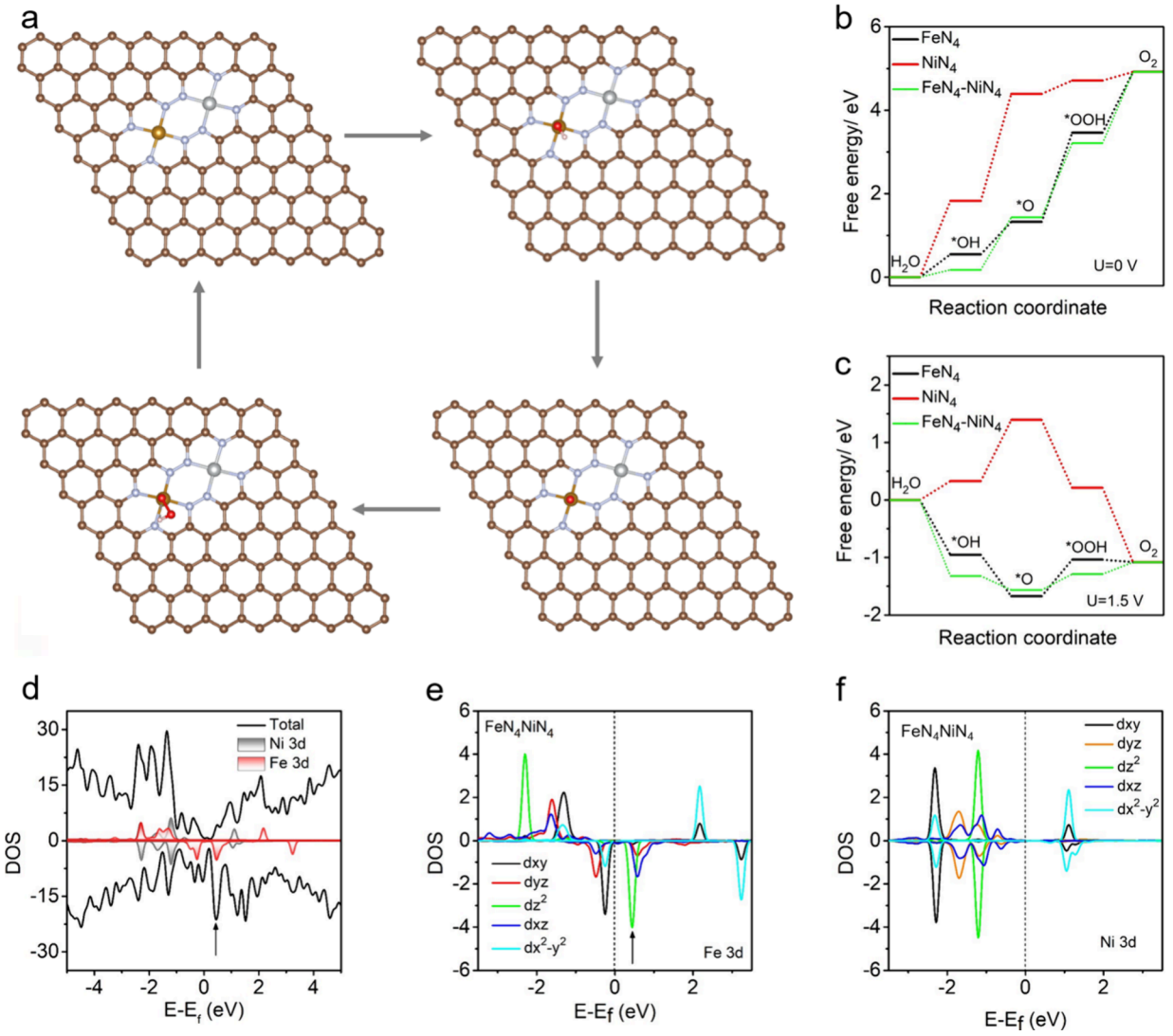

Figure 4. (a) OER pathway on FeN_4−NiN_4 sites. Free energy diagrams of FeN_4−NiN_4, FeN_4, and NiN_4 at (b) U = 0 and (c) U = 1.5 V, (d) PDOS plot of Fe and Ni 3d orbitals, and DOS of the five 3d orbitals of (e) Fe and (f) Ni.

are depicted in Figure 4a and Figures S8 and S9. Figure 4b and c shows the calculated free energy diagrams of three important reaction intermediates (i.e., *OH, *O, and *OOH) adsorbed on these metal sites at different applied voltages. At the applied voltage of U = 0 V, all four electron-transfer steps of the OER are endothermal, indicating a high energy barrier, whereas at a more positive voltage of U = 1.5 V, the rate-determining step (RDS) can be identified as the third electron transfer, the generation of *OOH on both FeN_4−NiN_4 and FeN_4. This step possesses a reaction free energy of 0.28 eV for FeN_4−NiN_4, which is 0.36 eV lower than that of FeN_4. This suggests that the introduction of adjacent NiN_4 can enhance the intrinsic activity of FeN_4 for OER.[29,30] In contrast, the RDS on the NiN_4 site is identified as the second electron-transfer step, the deprotonation of *OH, which necessitates a reaction free energy of 1.06 eV, considerably higher than those of the preceding two sites. This suggests that the FeN_4 site is the dominant active center in catalyzing the OER.

Consistent results can be obtained from the calculations of the density of states (DOS) and Bader charge analysis. From Table S9, it can be seen that indeed the Fe site of FeN_4−NiN_4 is electron enriched whereas the Ni site becomes electron deficient, as compared to the monometallic FeN_4 and NiN_4, in agreement with results from the above XPS measurements. The DOS profiles are shown in Figure 4d, where the Fe atom can be seen to make the largest contribution to the DOS near the Fermi level (marked by a black arrow), confirming Fe to be the active site. The corresponding partial density of state (PDOS) profiles are displayed in Figure 4e, where the marked state of Fe atoms is related to the dz^2 orbitals, suggesting that the dz^2 electrons are more active than other 3d orbitals, in good agreement with the results reported in the literature.[18]

Taken together, these results suggest that the FeN_4−NiN_4 dual-site structure exhibits the most favorable configuration toward OER electrocatalysis, where the FeN_4 serves as the actual catalytic center, and the adjacent NiN_4 regulates the electronic environment of the Fe center through metal−metal charge transfer and hence enhances the OER activity of the FeN_4 sites. This is indeed manifested in the experimental measurements below.

OER Electrocatalysis and Alkaline Water Splitting. To assess the OER performance of the samples, linear scan voltammetry (LSV) tests were conducted on NCA/FeNi-500, NCA/Fe-500, and NCA/Ni-500, along with commercial

https://doi.org/10.1021/acssuschemeng.4c07297
ACS Sustainable Chem. Eng. 2025, 13, 311−320

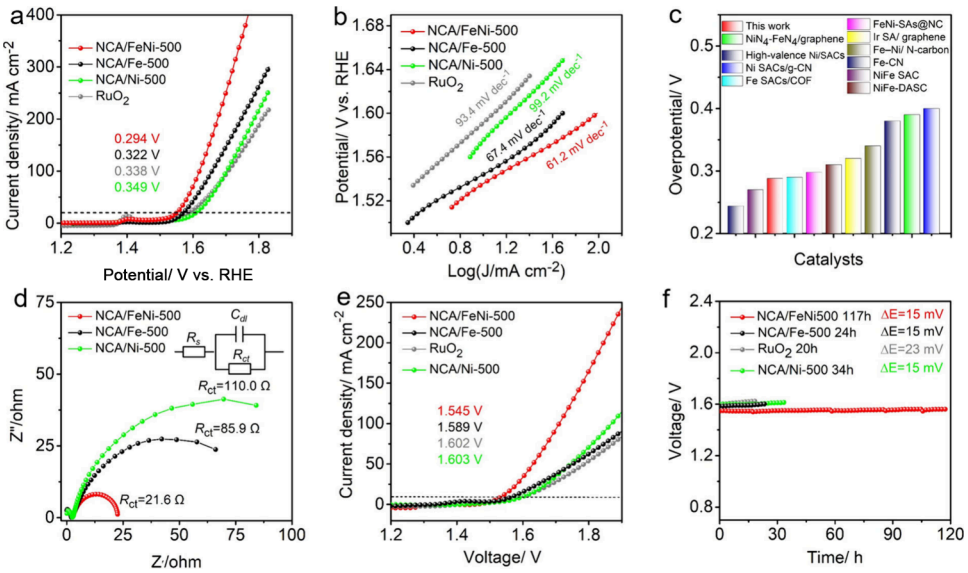

Figure 5. (a) OER polarization curves and (b) the corresponding Tafel plots of NCA/FeNi-500, NCA/Fe-500, NCA/Ni-500, and RuO_2 in 1.0 M KOH. (c) Comparison of the OER performance with relevant single- and dual-atom catalysts reported in the literature in 1.0 M KOH. (d) Nyquist plots of NCA/FeNi-500, NCA/Fe-500, and NCA/Ni-500. Inset shows the equivalent circuit where R_s is the serial resistance, R_{ct} the charge-transfer resistance, and C_{dl} the double-layer capacitance. (e) Current−voltage and (f) chronopotentiometric (at 10 mA cm^{-2}) curves of water splitting in 1.0 M KOH.

RuO_2. From Figure 5a, it can be seen that NCA/FeNi-500 exhibited the most favorable OER activity in 1.0 M KOH, with an overpotential (η_{10}) of only +294 mV to reach 10 mA cm^{-2}, significantly superior to those of commercial RuO_2 (+338 mV), NCA/Fe-500 (+322 mV), and NCA/Ni-500 (+349 mV). The corresponding Tafel slope was estimated to be 61.2 mV dec^{-1} for NCA/FeNi-500, notably lower than those of NCA/Fe-500 (67.4 mV dec^{-1}), NCA/Ni-500 (99.2 mV dec^{-1}), and RuO_2 (93.4 mV dec^{-1}) (Figure 5b). This indicates that NCA/FeNi-500 exhibits the best OER reaction kinetics among the series of catalysts, in good agreement with the results from the above DFT calculations. NCA/FeNi-500 also exhibited a superior OER performance, as compared to those of relevant OER catalysts reported recently in the literature (Figure 5c and Table S10).[14,31−39]

Consistently, in electrochemical impedance spectroscopy (Figure 5d), NCA/FeNi-500 can be seen to exhibit the lowest charge-transfer resistance (R_{ct}) of 21.6 Ω, in comparison to 85.9 Ω for NCA/Fe-500 and 110.0 Ω for NCA/Ni-500. The NCA/FeNi-500 also possessed the largest electrochemical active area (Figure S10) among the series, which was conducive to accessibility of the catalytic active centers.

Notably, NCA/FeNi-500 also stood out as the best catalyst among the samples prepared at different temperatures (Figure S11), suggesting that 500 °C was the optimal pyrolysis temperature. This is likely because a lower pyrolysis temperature resulted in a lower degree of graphitization of the carbon skeleton, whereas a higher pyrolysis temperature led to the aggregation of metal atoms, which reduced the number of metal single atom sites and thus the overall activity. In addition, from Figure S12, it can be seen that the OER activity of CA/FeNi-500, which was prepared by using EDTA instead of PM as the chelation ligands, was significantly lower than that of NCA/FeNi-500. This was likely due to significant agglomeration of metal species in CA/FeNi-500, as evidenced by the strong magnetic properties (Figure S13). In fact, from the XRD patterns in Figure S14, the formation of the magnetic alloy $FeNi_3$ could be readily resolved in the CA/FeNi-500 sample. This observation highlights the importance of nitrogen dopants in the carbon aerogels in facilitating atomic dispersion of the metal species, as M−O bonds are more prone to break than M−N bonds, during heat treatment.[40] Furthermore, in comparison to other bimetallic pairs in the carbon aerogels, such as NCA/FeCo-500 and NCA/NiCo-500 (Figure S15), NCA/FeNi-500 exhibited the best OER performance.[41]

To evaluate the catalytic activity and stability in practical applications, a two-electrode water electrolysis device was constructed using NCA/FeNi-500 or commercial RuO_2 as the anode catalyst, commercial Pt/C as the cathode catalyst, and 1.0 M KOH as the electrolyte. Pt/C is a well-known catalyst for the hydrogen evolution reaction (HER) (Figure S16). As illustrated in Figure 5e, the NCA/FeNi-500//Pt/C electrolyzer needed a voltage (E_{10}) of only 1.545 V to produce a current density of 10 mA cm^{-2} in water splitting, which is superior to those of RuO_2//Pt/C (1.602 V), NCA/Fe-500//Pt/C (1.589 V), and NCA/Ni-500//Pt/C (1.603 V). This confirmed the best performance of NCA/FeNi-500 in water splitting, which also exhibited the best durability, as made evident in chronopotentiometric measurements. From Figure 5f, one can see that to maintain a constant current density of 10 mA cm^{-2}, the RuO_2//Pt/C electrolyzer exhibited a voltage increase of 23 mV after 20 h of continuous operation, whereas NCA/FeNi-500//Pt/C showed a smaller increment of 15 mV even after 117 h of electrolysis. In fact, from Figure S17, it can be seen that the η_{10} of NCA/FeNi-500 increased by only 8 mV after 117 h of water electrolysis, in comparison to 15 mV for RuO_2 after only 20 h. It has been reported that demetalation and carbon oxidation are the key factors that cause the degradation of the electrocatalytic performance of metal, carbon-doped composites.[42] Thus, the remarkable stability of NCA/FeNi-500 can be attributed to the stable dual metal sites and the high resistance against oxidation of the carbon scaffold.

Alkaline Seawater Splitting. The NCA/FeNi-500 composites also exhibited remarkable OER activity for

https://doi.org/10.1021/acssuschemeng.4c07297
ACS Sustainable Chem. Eng. 2025, 13, 311−320

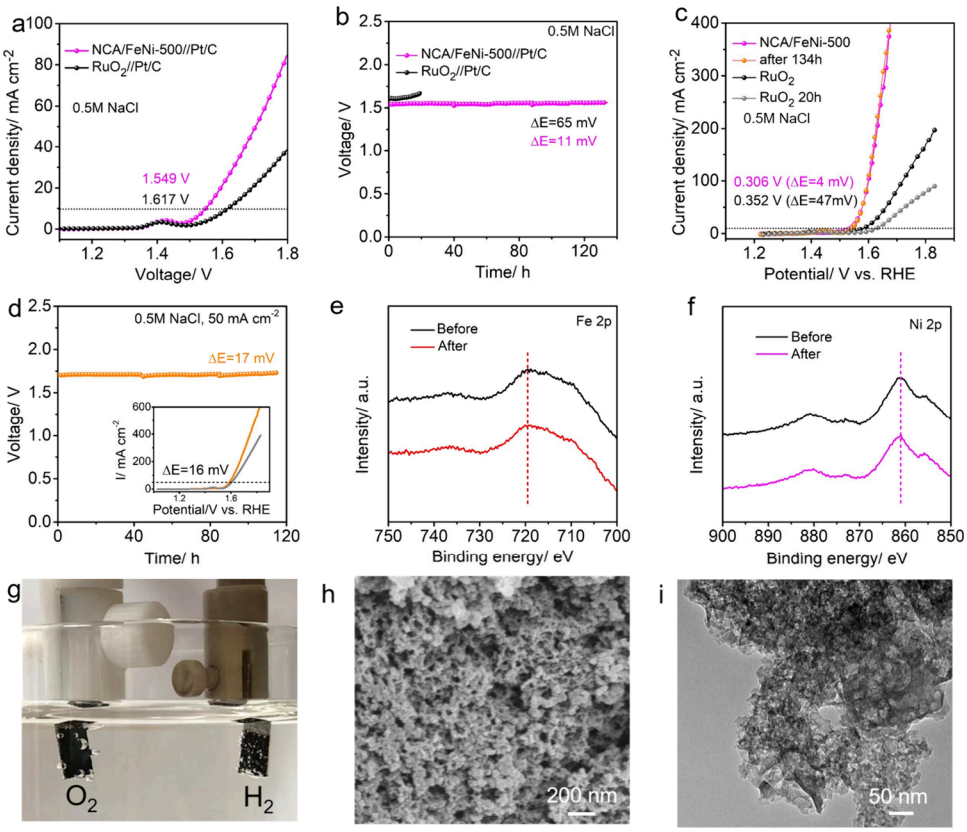

Figure 6. (a) Current−voltage curves of overall water splitting in simulated alkaline seawater. (b) Chronopotentiometric curves at a current density of 10 mA cm^{-2} with NCA/FeNi-500//Pt/C and RuO_2//Pt/C. (c) OER polarization curves before and after electrolysis in simulated alkaline seawater. (d) Chronopotentiometric curves at 50 mA cm^{-2} with NCA/FeNi-500//Pt/C. Inset shows the LSV curves of NCA/FeNi-500 before and after 115 h of electrolysis. The high-resolution scans of the (e) Fe 2p and (f) Ni 2p electrons of NCA/FeNi-500 before and after electrolysis in simulated seawater. (g) Photograph of water splitting with NCA/FeNi-500//Pt/C at 10 mA cm^{-2}. (h) SEM and (i) TEM images of NCA/FeNi-500 after electrolysis in simulated seawater.

seawater electrolysis. Figure 6a shows the electrolytic profiles of NCA/FeNi-500//Pt/C and RuO_2//Pt/C in simulated alkaline seawater with a 0.5 M NaCl + 1.0 M KOH solution (where Pt/C again exhibited a notable HER performance, Figure S18). It can be observed that NCA/FeNi-500//Pt/C was capable of reaching a current density of 10 mA cm^{-2} with a voltage of only 1.549 V, markedly better than that of RuO_2//Pt/C (1.617 V), producing a large number of H_2 and O_2 bubbles (Figure 6g). In comparison to the response in 1 M KOH electrolyte, the cell voltage increased by only 12 mV for NCA/FeNi-500 in simulated alkaline seawater, suggesting minimal impacts of the solution salinity and chlorine evolution reaction. This suggests that NCA/FeNi-500 was suitable for use in alkaline seawater electrolysis.[43,44] In the stability tests at 10 mA cm^{-2} (Figure 6b), it can be observed that RuO_2//Pt/C exhibited severe deactivation after 22 h of continuous operation, whereas the catalytic activity of NCA/FeNi-500 remained largely unchanged even after 134 h, where E_{10} increased by only 4 mV, in comparison to 47 mV for RuO_2 after only 22 h (Figure 6c). Notably, after electrolysis for 115 h at a higher current density of 50 mA cm^{-2}, LSV measurements showed that the η_{10} of NCA/FeNi-500 increased by merely 16 mV (Figure 6d and inset). Additionally, NCA/FeNi-500 exhibited a Tafel slope of 59.7 mV dec^{-1} for the OER (Figure S19), much lower than that of RuO_2 (92.2 mV dec^{-1}), indicating that NCA/FeNi-500 could sustain excellent reaction kinetics even in simulated alkaline seawater electrolysis.

To investigate the changes of the carbon aerogel skeleton and FeNi metal species before and after simulated alkaline seawater electrolysis, we performed XPS measurements of the NCA/FeNi-500 sample. As shown in Figure S20 and Table S11, the elemental compositions of NCA/FeNi-500 remained largely unchanged, suggesting minimal impacts of Cl^- ions on the catalyst structure. In addition, as shown in Figure 6e and f, the binding energies of Fe and Ni also remained virtually invariant, suggesting that the FeN_4−NiN_4 sites were not deactivated by Cl^-. Consistent results were obtained in TEM and SEM measurements (Figure 6h, i), where NCA/FeNi-500 can be seen to retain an intact honeycomb porous structure after electrolysis and the carbon skeleton was not damaged.

The remarkable stability of NCA/FeNi-500 even in the Cl^- rich environments might be ascribed to the strong interactions between the metal species and the carbon substrate. Meanwhile, the rich pore size structure of the carbon aerogel enabled the catalyst to have a large specific surface area and provided abundant mass transfer channels for the gases generated in the catalytic process, which efficiently minimized the impact of gas flushing on the catalyst.

CONCLUSION

In summary, carbon aerogels embedded with iron−nickel dual metal sites (NCA/FeNi-500) were prepared by controlled pyrolysis of chitosan hydrogel composite which possessed a metal loading up to 4.35 wt %. Microscopic and spectroscopic

https://doi.org/10.1021/acssuschemeng.4c07297
ACS Sustainable Chem. Eng. 2025, 13, 311−320

measurements suggested that the metal species were atomically dispersed into the carbon scaffold in the forms of adjacent FeN_4 and NiN_4 moieties with apparent Ni to Fe electron transfer. Results from DFT calculations indicated that the FeN_4−NiN_4 dual-site configuration exhibited the most favorable catalytic activity toward OER, with FeN_4 serving as the primary active center. In electrochemical measurements, NCA/FeNi-500 indeed exhibited a remarkable OER activity in both alkaline water and simulated alkaline seawater, featuring a low η_{10} of only +294 and +306 mV, much better than those of the monometallic counterparts and commercial RuO_2, along with much enhanced stability. The highly effective OER activity and stability of NCA/FeNi-500 were also manifested in electrolysis in alkaline media and simulated alkaline seawater. These results put forward a facile strategy in the preparation of carbon-based nanocomposites with dense atomic metal sites for electrochemical energy conversion and storage.

■ ASSOCIATED CONTENT

Supporting Information

The Supporting Information is available free of charge at https://pubs.acs.org/doi/10.1021/acssuschemeng.4c07297.

Additional experimental details and experimental data (PDF)

■ AUTHOR INFORMATION

Corresponding Authors

Yang Liu − *College of Chemistry and Chemical Engineering, Central South University, Changsha 410083, China*; Email: lyaccsu@163.com

Shaowei Chen − *Department of Chemistry and Biochemistry, University of California, Santa Cruz, California 95064, United States*; orcid.org/0000-0002-3668-8551; Email: shaowei@ucsc.edu

Ting He − *School of Materials Science and Engineering, Xiangtan University, Xiangtan 411105 Hunan, China*; orcid.org/0000-0003-2854-1645; Email: heting891020@csu.edu.cn

Authors

Linshu Shan − *School of Materials Science and Engineering, Xiangtan University, Xiangtan 411105 Hunan, China*

Yang Chen − *Key Laboratory of Functional Metal−Organic Compounds of Hunan Province, College of Chemistry and Materials Science, Hengyang Normal University, Hengyang 421008, P. R. China*

Xinjie Zhang − *School of Materials Science and Engineering, Xiangtan University, Xiangtan 411105 Hunan, China*

Haizhong Dai − *School of Materials Science and Engineering, Xiangtan University, Xiangtan 411105 Hunan, China*

Dahai Xu − *School of Materials Science and Engineering, Xiangtan University, Xiangtan 411105 Hunan, China*

Bingzhe Yu − *Department of Chemistry and Biochemistry, University of California, Santa Cruz, California 95064, United States*

Yi Zhang − *College of Chemistry and Chemical Engineering, Central South University, Changsha 410083, China*; orcid.org/0000-0002-8452-9694

Xiaoping Ouyang − *School of Materials Science and Engineering, Xiangtan University, Xiangtan 411105 Hunan, China*

Complete contact information is available at: https://pubs.acs.org/10.1021/acssuschemeng.4c07297

Author Contributions

#L.S. and Y.L. contributed equally. The manuscript was written through contributions of all authors. All authors have given approval to the final version of the manuscript.

Notes

The authors declare no competing financial interest.

■ ACKNOWLEDGMENTS

T.H. is thankful for Xiangtan University Scientific Research Project Funding (No. 22QDZ51) and the Hunan Natural Science Foundation (No. 2024JJ6421). S.C. thanks the National Science Foundation for partial support of the work (CHE-1900235 and CHE-2003685). Y.C. acknowledges support from the Youth Program of Nature Science Foundation of Hunan Province (2024JJ6098), the Innovation Platform Open Fund of Hengyang Normal University (2023HSKFJJ006), and the Scientific Research Fund of Hengyang Normal University (2023QD19). The authors also thank Eceshi (www.eceshi.com) and the High-Performance Computing Center of CSU for assistance in the computational studies.

■ REFERENCES

(1) Qin, R.; Chen, G.; Feng, X.; Weng, J.; Han, Y. Ru/Ir-Based Electrocatalysts for Oxygen Evolution Reaction in Acidic Conditions: From Mechanisms, Optimizations to Challenges. *Adv. Sci.* **2024**, *11* (21), No. 2309364.

(2) Wei, J.; Tang, H.; Sheng, L.; Wang, R.; Fan, M.; Wan, J.; Wu, Y.; Zhang, Z.; Zhou, S.; Zeng, J. Site-specific metal-support interaction to switch the activity of Ir single atoms for oxygen evolution reaction. *Nat. Commun.* **2024**, *15* (1), 559.

(3) Magnier, L.; Cossard, G.; Martin, V.; Pascal, C.; Roche, V.; Sibert, E.; Shchedrina, I.; Bousquet, R.; Parry, V.; Chatenet, M. Fe−Ni-based alloys as highly active and low-cost oxygen evolution reaction catalyst in alkaline media. *Nat. Mater.* **2024**, *23* (2), 252−261.

(4) Chen, Y.; Mao, J.; Zhou, H.; Xing, L.; Qiao, S.; Yuan, J.; Mei, B.; Wei, Z.; Zhao, S.; Tang, Y.; Liu, C. Coordination Shell Dependent Activity of CuCo Diatomic Catalysts for Oxygen Reduction, Oxygen Evolution, and Hydrogen Evolution Reaction. *Adv. Funct. Mater.* **2024**, *34* (10), No. 2311664.

(5) Li, Q.; He, T.; Jiang, X.; Lei, Y.; Liu, Q.; Liu, C.; Sun, Z.; Chen, S.; Zhang, Y. Boosting oxygen evolution activity of nickel iron hydroxide by iron hydroxide colloidal particles. *J. Colloid Interface Sci.* **2022**, *606*, 518−525.

(6) He, T.; Song, Y.; Chen, Y.; Song, X.; Lu, B.; Liu, Q.; Liu, H.; Zhang, Y.; Ouyang, X.; Chen, S. Atomically dispersed ruthenium in carbon aerogels as effective catalysts for pH-universal hydrogen evolution reaction. *Chem. Eng. J.* **2022**, *442*, No. 136337.

(7) He, T.; Lu, B.; Chen, Y.; Wang, Y.; Zhang, Y.; Davenport, J. L.; Chen, A. P.; Pao, C.-W.; Liu, M.; Sun, Z. Nanowrinkled Carbon Aerogels Embedded with FeNx Sites as Effective Oxygen Electrodes for Rechargeable Zinc-Air Battery. *Research* **2019**, *2019*, 6813585.

(8) Chen, Y.; Hu, S.; Nichols, F.; Bridges, F.; Kan, S.; He, T.; Zhang, Y.; Chen, S. Carbon aerogels with atomic dispersion of binary iron−cobalt sites as effective oxygen catalysts for flexible zinc−air batteries. *J. Mater. Chem. A* **2020**, *8* (23), 11649−11655.

(9) Ye, G.; He, Q.; Liu, S.; Zhao, K.; Su, Y.; Zhu, W.; Huang, R.; He, Z. Cage-confinement of gas-phase ferrocene in zeolitic imidazolate frameworks to synthesize high-loading and atomically dispersed Fe−N codoped carbon for efficient oxygen reduction reaction. *J. Mater. Chem. A* **2019**, *7* (27), 16508−16515.

(10) Jiao, L.; Zhang, R.; Wan, G.; Yang, W.; Wan, X.; Zhou, H.; Shui, J.; Yu, S.-H.; Jiang, H.-L. Nanocasting SiO2 into metal−organic

frameworks imparts dual protection to high-loading Fe single-atom electrocatalysts. *Nat. Commun.* **2020**, *11* (1), 2831.
(11) Hai, X.; Xi, S.; Mitchell, S.; Harrath, K.; Xu, H.; Akl, D. F.; Kong, D.; Li, J.; Li, Z.; Sun, T.; Yang, H.; Cui, Y.; Su, C.; Zhao, X.; Li, J.; Pérez-Ramírez, J.; Lu, J. Scalable two-step annealing method for preparing ultra-high-density single-atom catalyst libraries. *Nat. Nanotechnol.* **2022**, *17* (2), 174−181.
(12) Jiao, L.; Li, J.; Richard, L. L.; Sun, Q.; Stracensky, T.; Liu, E.; Sougrati, M. T.; Zhao, Z.; Yang, F.; Zhong, S.; Xu, H.; Mukerjee, S.; Huang, Y.; Cullen, D. A.; Park, J. H.; Ferrandon, M.; Myers, D. J.; Jaouen, F.; Jia, Q. Chemical vapour deposition of Fe−N−C oxygen reduction catalysts with full utilization of dense Fe−N4 sites. *Nat. Mater.* **2021**, *20* (10), 1385−1391.
(13) Li, H.; Wang, J.; Qi, R.; Hu, Y.; Zhang, J.; Zhao, H.; Zhang, J.; Zhao, Y. Enhanced Fe 3d delocalization and moderate spin polarization in FeNi atomic pairs for bifunctional ORR and OER electrocatalysis. *Appl. Catal., B* **2021**, *285*, No. 119778.
(14) Chen, J.; Li, H.; Fan, C.; Meng, Q.; Tang, Y.; Qiu, X.; Fu, G.; Ma, T. Dual Single-Atomic Ni-N4 and Fe-N4 Sites Constructing Janus Hollow Graphene for Selective Oxygen Electrocatalysis. *Adv. Mater.* **2020**, *32* (30), No. 2003134.
(15) Jiao, L.; Zhu, J.; Zhang, Y.; Yang, W.; Zhou, S.; Li, A.; Xie, C.; Zheng, X.; Zhou, W.; Yu, S.-H.; Jiang, H.-L. Non-Bonding Interaction of Neighboring Fe and Ni Single-Atom Pairs on MOF-Derived N-Doped Carbon for Enhanced CO2 Electroreduction. *J. Am. Chem. Soc.* **2021**, *143* (46), 19417−19424.
(16) Li, Q.; Sun, Z.; Yin, C.; Chen, Y.; Pan, D.; Yu, B.; Zhang, Y.; He, T.; Chen, S. Template-assisted synthesis of ultrathin graphene aerogels as bifunctional oxygen electrocatalysts for water splitting and alkaline/neutral zinc-air batteries. *Chem. Eng. J.* **2023**, *458*, No. 141492.
(17) Wan, C.; Duan, X.; Huang, Y. Molecular Design of Single-Atom Catalysts for Oxygen Reduction Reaction. *Adv. Energy Mater.* **2020**, *10* (14), No. 1903815.
(18) He, T.; Chen, Y.; Liu, Q.; Lu, B.; Song, X.; Liu, H.; Liu, M.; Liu, Y.-N.; Zhang, Y.; Ouyang, X.; Chen, S. Theory-Guided Regulation of FeN4 Spin State by Neighboring Cu Atoms for Enhanced Oxygen Reduction Electrocatalysis in Flexible Metal-Air Batteries. *Angew. Chem., Int. Ed.* **2022**, *61* (27), No. e202201007.
(19) Wang, P.; Hayashi, T.; Meng, Q. a.; Wang, Q.; Liu, H.; Hashimoto, K.; Jiang, L. Highly Boosted Oxygen Reduction Reaction Activity by Tuning the Underwater Wetting State of the Superhydrophobic Electrode. *Small* **2017**, *13* (4), na DOI: 10.1002/smll.201601250.
(20) Bai, L.; Hsu, C.-S.; Alexander, D. T. L.; Chen, H. M.; Hu, X. A Cobalt−Iron Double-Atom Catalyst for the Oxygen Evolution Reaction. *J. Am. Chem. Soc.* **2019**, *141* (36), 14190−14199.
(21) Xue, H.; He, T.; Chabu, J. M.; Liu, J.; Wu, H.; Zheng, J.; Tan, M.; Ma, J.; Shen, R.; Deng, L.; Zhang, Y. Iron single clusters anchored on N-doped porous carbon as superior trace-metal catalysts toward oxygen reduction. *Adv. Mater. Interfaces* **2018**, *5* (7), No. 1701345.
(22) Boppella, R.; Austeria P, M.; Kim, Y.; Kim, E.; Song, I.; Eom, Y.; Kumar, D. P.; Balamurugan, M.; Sim, E.; Kim, D. H.; Kim, T. K. Pyrrolic N-Stabilized Monovalent Ni Single-Atom Electrocatalyst for Efficient CO2 Reduction: Identifying the Role of Pyrrolic−N and Synergistic Electrocatalysis. *Adv. Funct. Mater.* **2022**, *32* (35), No. 2202351.
(23) Zeng, Y.; Li, C.; Li, B.; Liang, J.; Zachman, M. J.; Cullen, D. A.; Hermann, R. P.; Alp, E. E.; Lavina, B.; Karakalos, S.; Lucero, M.; Zhang, B.; Wang, M.; Feng, Z.; Wang, G.; Xie, J.; Myers, D. J.; Dodelet, J.-P.; Wu, G. Tuning the thermal activation atmosphere breaks the activity−stability trade-off of Fe−N−C oxygen reduction fuel cell catalysts. *Nature Catal.* **2023**, *6* (12), 1215−1227.
(24) Zang, Y.; Lu, D.-Q.; Wang, K.; Li, B.; Peng, P.; Lan, Y.-Q.; Zang, S.-Q. A pyrolysis-free Ni/Fe bimetallic electrocatalyst for overall water splitting. *Nat. Commun.* **2023**, *14* (1), 1792.
(25) Chen, Y.; Ji, S.; Wang, Y.; Dong, J.; Chen, W.; Li, Z.; Shen, R.; Zheng, L.; Zhuang, Z.; Wang, D.; Li, Y. Isolated single iron atoms anchored on N-doped porous carbon as an efficient electrocatalyst for the oxygen reduction reaction. *Angew. Chem., Int. Ed.* **2017**, *56* (24), 6937−6941.
(26) Niu, H.; Huang, L.; Qin, Y.; Qi, R.; Mei, B.; Wu, D.; Li, F.-M.; You, B.; Li, Q.; Yao, Y.; Wang, Z.; Yao, T.; Ding, S.; Guo, W.; Chen, Y.; Su, Y.; Song, F.; Xia, B. Y. Hydrogen Peroxide Spillover on Platinum−Iron Hybrid Electrocatalyst for Stable Oxygen Reduction. *J. Am. Chem. Soc.* **2024**, *146* (32), 22650−22660.
(27) Yin, S.; Yi, H.; Liu, M.; Yang, J.; Yang, S.; Zhang, B.-W.; Chen, L.; Cheng, X.; Huang, H.; Huang, R.; Jiang, Y.; Liao, H.; Sun, S. An in situ exploration of how Fe/N/C oxygen reduction catalysts evolve during synthesis under pyrolytic conditions. *Nat. Commun.* **2024**, *15* (1), 6229.
(28) Hua, W.; Sun, H.; Lin, L.; Mu, Q.; Yang, B.; Su, Y.; Wu, H.; Lyu, F.; Zhong, J.; Deng, Z.; Peng, Y. A hierarchical Single-Atom Ni-N3-C catalyst for electrochemical CO2 reduction to CO with Near-Unity faradaic efficiency in a broad potential range. *Chem. Eng. J.* **2022**, *446*, No. 137296.
(29) Cui, T.; Liu, Q.; Chen, S. Dual-Atom Catalysts for Electrochemical Energy Technologies. *Energy Technology* **2023**, *11* (4), No. 2201456.
(30) Lu, B. Z.; Liu, Q. M.; Wang, C. Y.; Masood, Z.; Morris, D. J.; Nichols, F.; Mercado, R.; Zhang, P.; Ge, Q. F.; Xin, H. L. L.; Chen, S. W. Ultrafast Preparation of Nonequilibrium FeNi Spinels by Magnetic Induction Heating for Unprecedented Oxygen Evolution Electrocatalysis. *Research* **2022**, *2022*, No. 9756983.
(31) Li, X.; Su, Z.; Zhao, Z.; Cai, Q.; Li, Y.; Zhao, J. Single Ir atom anchored in pyrrolic-N4 doped graphene as a promising bifunctional electrocatalyst for the ORR/OER: a computational study. *J. Colloid Interface Sci.* **2022**, *607*, 1005−1013.
(32) Li, Y.; Wu, Z.-S.; Lu, P.; Wang, X.; Liu, W.; Liu, Z.; Ma, J.; Ren, W.; Jiang, Z.; Bao, X. High-Valence Nickel Single-Atom Catalysts Coordinated to Oxygen Sites for Extraordinarily Activating Oxygen Evolution Reaction. *Adv. Sci.* **2020**, *7* (5), No. 1903089.
(33) Lu, S.; Huynh, H. L.; Lou, F.; Guo, K.; Yu, Z. Single transition metal atom embedded antimonene monolayers as efficient trifunctional electrocatalysts for the HER, OER and ORR: a density functional theory study. *Nanoscale* **2021**, *13* (30), 12885−12895.
(34) Luo, F.; Zhu, J.; Ma, S.; Li, M.; Xu, R.; Zhang, Q.; Yang, Z.; Qu, K.; Cai, W.; Chen, Z. Regulated coordination environment of Ni single atom catalyst toward high-efficiency oxygen electrocatalysis for rechargeable Zinc-air batteries. *Energy Storage Mater.* **2021**, *35*, 723−730.
(35) Lv, X.; Wei, W.; Wang, H.; Huang, B.; Dai, Y. Holey graphitic carbon nitride (g-CN) supported bifunctional single atom electrocatalysts for highly efficient overall water splitting. *Appl. Catal., B* **2020**, *264*, No. 118521.
(36) Wan, W.; Zhao, Y.; Wei, S.; Triana, C. A.; Li, J.; Arcifa, A.; Allen, C. S.; Cao, R.; Patzke, G. R. Mechanistic insight into the active centers of single/dual-atom Ni/Fe-based oxygen electrocatalysts. *Nat. Commun.* **2021**, *12* (1), 5589.
(37) Wang, X.; Sun, L.; Zhou, W.; Yang, L.; Ren, G.; Wu, H.; Deng, W.-Q. Iron single-atom catalysts confined in covalent organic frameworks for efficient oxygen evolution reaction. *Cell Rep. Phys. Sci.* **2022**, *3* (3), No. 100804.
(38) Zeng, Z.; Gan, L. Y.; Bin Yang, H.; Su, X.; Gao, J.; Liu, W.; Matsumoto, H.; Gong, J.; Zhang, J.; Cai, W.; Zhang, Z.; Yan, Y.; Liu, B.; Chen, P. Orbital coupling of hetero-diatomic nickel-iron site for bifunctional electrocatalysis of CO2 reduction and oxygen evolution. *Nat. Commun.* **2021**, *12* (1), 4088.
(39) Zhu, X.; Zhang, D.; Chen, C.-J.; Zhang, Q.; Liu, R.-S.; Xia, Z.; Dai, L.; Amal, R.; Lu, X. Harnessing the interplay of Fe−Ni atom pairs embedded in nitrogen-doped carbon for bifunctional oxygen electrocatalysis. *Nano Energy* **2020**, *71*, No. 104597.
(40) Ji, J.; Hou, Y.; Zhou, S.; Qiu, T.; Zhang, L.; Ma, L.; Qian, C.; Zhou, S.; Liang, C.; Ling, M. Oxygen-coordinated low-nucleus cluster catalysts for enhanced electrocatalytic water oxidation. *Carbon Energy* **2023**, *5* (2), No. e216.

(41) Sun, H.; Yan, Z.; Liu, F.; Xu, W.; Cheng, F.; Chen, J. Self-Supported Transition-Metal-Based Electrocatalysts for Hydrogen and Oxygen Evolution. *Adv. Mater.* **2020**, *32* (3), No. 1806326.
(42) Li, J.; Sougrati, M. T.; Zitolo, A.; Ablett, J. M.; Oğuz, I. C.; Mineva, T.; Matanovic, I.; Atanassov, P.; Huang, Y.; Zenyuk, I.; Di Cicco, A.; Kumar, K.; Dubau, L.; Maillard, F.; Dražić, G.; Jaouen, F. Identification of durable and non-durable FeNx sites in Fe−N−C materials for proton exchange membrane fuel cells. *Nat. Catal.* **2021**, *4*, 10−19.
(43) Liu, H.; Shen, W.; Jin, H.; Xu, J.; Xi, P.; Dong, J.; Zheng, Y.; Qiao, S.-Z. High-Performance Alkaline Seawater Electrolysis with Anomalous Chloride Promoted Oxygen Evolution Reaction. *Angew. Chem., Int. Ed.* **2023**, *62* (46), No. e202311674.
(44) Ning, M.; Zhang, F.; Wu, L.; Xing, X.; Wang, D.; Song, S.; Zhou, Q.; Yu, L.; Bao, J.; Chen, S.; Ren, Z. Boosting efficient alkaline fresh water and seawater electrolysis via electrochemical reconstruction. *Energy Environ. Sci.* **2022**, *15* (9), 3945−3957.

https://doi.org/10.1021/acssuschemeng.4c07297
ACS Sustainable Chem. Eng. 2025, 13, 311−320